

# Hover Flight Control Design for UAS Using Performance-based Disturbance Rejection Requirements

**Marcos G. Berrios**

**Tom Berger**

**Mark B. Tischler**

U.S. Army Aviation Development Directorate  
Moffett Field, CA, USA

**Ondrej Juhasz**

**Frank C. Sanders**

San Jose State University  
Research Foundation  
Moffett Field, CA, USA

## ABSTRACT

A key class of UAS are VTOL vehicles, which afford the ability to hover and maneuver in tight spaces; often in windy and turbulent conditions. This paper presents the development and flight testing of optimized control laws for the 3DR IRIS+ quadrotor designed to aggressively hold its position in a hover while subjected to wind gusts and turbulence. Performance-based disturbance rejection requirements, such as attitude/position tracking error in turbulence and maximum position displacement for a 1-cosine gust, are directly incorporated into the flight control design and optimization process. A Control Equivalent Turbulence Input (CETI) was then used to simulate turbulence in flight and the optimized control laws allowed for the quadrotor to hold its position to within 3.5 inches, a factor of 13.5 improvement over the stock position hold controller.

## NOTATION

$S_{\delta_{lat}}$	Inner-Loop Input Sensitivity	$\omega_c$	Crossover Frequency, rad/sec
$S_{\phi_{ref}}$	Outer-Loop Input Sensitivity	$\zeta$	Damping Ratio
$v_d$	Lateral Velocity Disturbance, ft/sec	<i>ACAH</i>	Attitude Command Attitude Hold
$v_g$	Lateral Gust Input, ft/sec	<i>ADD</i>	Aviation Development Directorate
$v_y$	Lateral velocity, ft/sec	<i>ADS</i>	Aeronautical Design Standard
$x$	Longitudinal Position, ft	<i>CDRB</i>	Control Equivalent Disturbance Rejection Bandwidth, rad/sec
$x_e$	Longitudinal Position Error, ft	<i>CDRP</i>	Control Equivalent Disturbance Rejection Peak, dB
$y$	Lateral Position, ft	<i>CETI</i>	Control Equivalent Turbulence Input
$y_d$	Lateral Position Disturbance, ft	<i>DRB</i>	Disturbance Rejection Bandwidth, rad/sec
$y_e$	Lateral Position Error, ft	<i>DRP</i>	Disturbance Rejection Peak, dB
$\delta_d$	Input Disturbance	<i>GM</i>	Gain Margin, dB
$\delta_{lat}$	Lateral Input	<i>MIMO</i>	Multi-Input Multi-Output
$p$	Roll Rate, deg/sec	<i>MTE</i>	Mission Take Element
$p_d$	Roll Rate Disturbance, deg/sec	<i>PBDR</i>	Performance-based Disturbance Rejection
$p_e$	Roll Rate Error, deg/sec	<i>PH</i>	Position Hold
$\phi$	Roll Attitude, deg	<i>PM</i>	Phase Margin, deg
$\phi_e$	Roll Attitude Error, deg	<i>RMS</i>	Root Mean Square
$\theta$	Pitch Attitude, deg	<i>UAS</i>	Unmanned Aerial System
$\theta_d$	Pitch Attitude Disturbance, deg	<i>VTOL</i>	Vertical Take-Off and Landing
$\theta_e$	Pitch Attitude Error, deg		
$\omega_{BW}$	-135 deg Phase Bandwidth, rad/sec		

Presented at the AHS 73rd Annual Forum, Fort Worth, Texas, May 9–11, 2017. This is work of the U.S. Government and is not subject to copyright protection in the U.S. Distribution A. Approved for public release; distribution is unlimited.

## INTRODUCTION

Unmanned aerial systems (UAS) play an increasingly significant role in military, commercial, and recreational aviation. A key class of UAS are vertical take-off and landing (VTOL) vehicles, which afford the ability to hover and ma-

neuver in tight spaces; often in windy and turbulent conditions.

Various methods have been proposed to develop flight control systems for VTOL UAS that are capable of rejecting wind gusts and turbulence. These methods include using angular acceleration feedback to allow for increased gains and bandwidth (Ref. 1), tuning of PID controllers to minimize the magnitude of the input disturbance sensitivity function (Ref. 2), estimating wind velocity in flight and eliminating its effect using feedback (Ref. 3), and identifying turbulent airwake spectral properties online for use in an adaptive gust alleviating control law (Ref. 4).

Unlike manned aircraft, where handling qualities and pilot subjectivity are important, UAS are inherently performance driven vehicles. For manned aircraft, Mission Task Elements (MTEs) are used to assess the handling qualities via assigned Cooper-Harper Handling Quality Ratings (HQR) (Ref. 5). By definition, MTEs have very specific performance level boundaries. For example, the pilot must maintain the helicopter positioned within  $\pm 3$  ft of a point on the ground to achieve a Level 1 rating for the Hover MTE. Consequently, without pilot subjectivity, assessing flying qualities becomes purely *performance driven*.

Performance-based disturbance rejection (PBDR) requirements have been used to design control laws for a UH-60. Specifically, a stability augmentation system for operation in a ship airwake has been designed by minimizing the power spectrum density of the transfer function between the gust input and aircraft rate responses (Ref. 6). In addition, a PBDR requirement of holding a specified position tolerance in moderate turbulence has been used to tune and flight test outer-loop position hold control laws for a UH-60 (Ref. 7). This paper expands on the previous work by incorporating similar and additional PBDR requirements into the flight control design and optimization process for UAS in hover.

The objectives of this research are two-fold. The first objective is to design a control system for a quadrotor that aggressively holds a position over the ground in the presence of wind gusts and turbulence. This objective is accomplished by using the flight control design and optimization methods developed at the Aviation Development Directorate for manned aircraft (Ref. 8) and by including performance-based disturbance rejection requirements directly into the flight control design and optimization process. Two such requirements used in the optimization process are the attitude/position tracking error while hovering in turbulence and the maximum position displacement when subjected to a 1-cosine gust (Ref. 9).

The second objective is to use the proposed performance-based approach to design flight control systems with various levels of disturbance rejection characteristics and correlate quantitative performance with existing flying qualities and flight control specifications (e.g., stability margins, crossover frequencies, disturbance rejection bandwidth, etc.).

## DISTURBANCE REJECTION

Both random turbulence and discrete gusts are types of process disturbances. The effect of these disturbances on an aircraft's combined dynamics and control system can be quantified by examining the block diagram interaction between the two. Figure 1 depicts a typical roll attitude command block diagram with pre-filter,  $\mathbf{P}_\phi$ , controller  $\mathbf{K}_\phi$ , input disturbance filter  $D(s)$ , and plant  $\mathbf{G}_\phi$ .

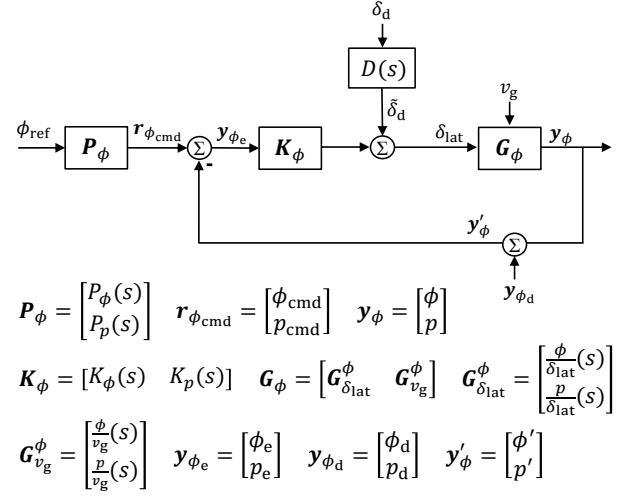


Fig. 1. A typical roll attitude feedback block diagram.

The error dynamics  $\mathbf{y}_{\phi_e}$  can be expressed as a function of the reference input  $\phi_{\text{ref}}$ , the input disturbance  $\delta_d$ , and the lateral gust  $v_g$  as:

$$\mathbf{y}_{\phi_e} = \mathbf{P}_\phi \cdot \phi_{\text{ref}} - \mathbf{S}_\phi \mathbf{G}_{\delta_{\text{lat}}}^\phi D(s) \cdot \delta_d - \mathbf{S}_\phi \mathbf{G}_{v_g}^\phi \cdot v_g \quad (1)$$

where  $\mathbf{S}_\phi$  is the matrix of sensitivity functions:

$$\mathbf{S}_\phi = (\mathbf{I} + \mathbf{G}_{\delta_{\text{lat}}}^\phi \mathbf{K}_\phi)^{-1} = \begin{bmatrix} S_{\phi\phi}(s) & S_{pp}(s) \\ S_{\phi p}(s) & S_{pp}(s) \end{bmatrix} \quad (2)$$

The attitude sensitivity function  $S_{\phi\phi}$ , as used in classical MIMO design, is also referred to as the roll attitude disturbance rejection frequency response (Ref. 10). This response corresponds to the roll attitude output due to a roll attitude disturbance at the sensor measurement:

$$S_{\phi\phi}(s) = \frac{\phi'}{\phi_d}(s) \quad (3)$$

In general,  $S_{ij}$  corresponds to the response  $j$  for an input  $i$  at the sensor measurement.

Setting the reference input to zero isolates the effect of the input disturbance and gust on the error and yields:

$$\mathbf{y}_{\phi_e} = -\mathbf{S}_\phi (\mathbf{G}_{\delta_{\text{lat}}}^\phi D(s) \cdot \delta_d + \mathbf{G}_{v_g}^\phi \cdot v_g) \quad (4)$$

Of specific interest for this attitude command controller is the attitude error  $\phi_e$  due to an input disturbance and gust

which is given by:

$$\phi_e = -(S_{\phi\phi}(s) + s \cdot S_{p\phi}(s)) \cdot \left(\frac{\phi}{\delta_{\text{lat}}}(s) \cdot D(s) \cdot \delta_d + \frac{\phi}{v_g}(s) \cdot v_g\right) \quad (5)$$

where the expression  $(S_{\phi\phi}(s) + s \cdot S_{p\phi}(s))$  is the input sensitivity transfer function:

$$S_{\delta_{\text{lat}}}(s) \triangleq \frac{\delta_{\text{lat}}}{\delta_d}(s) = (S_{\phi\phi}(s) + s \cdot S_{p\phi}(s)) \quad (6)$$

and it is assumed that  $p = s \cdot \phi$ . Further simplification of Equation 5 yields:

$$\phi_e = -S_{\delta_{\text{lat}}}(s) \cdot \left(\frac{\phi}{\delta_{\text{lat}}}(s) \cdot D(s) \cdot \delta_d + \frac{\phi}{v_g}(s) \cdot v_g\right) \quad (7)$$

Given an input disturbance filter  $D(s)$ , and assuming that the plant dynamics  $\phi/\delta_{\text{lat}}$  and  $\phi/v_g$  do not change, the input sensitivity function  $S_{\delta_{\text{lat}}}$  directly shows the effect of feedback on  $\phi_e$  in the presence of an input disturbance  $\delta_d$  and gust  $v_g$ . A typical input sensitivity frequency response is shown in Figure 2. Disturbances with frequencies such that  $|S_{\delta_{\text{lat}}}(j\omega)| < 0$  dB are attenuated by feedback, however, disturbances with frequencies such that  $|S_{\delta_{\text{lat}}}(j\omega)| > 0$  dB are amplified. Therefore, it is important to shape the sensitivity response such that maximum attenuation is achieved around the frequency range in which the disturbance is most active.

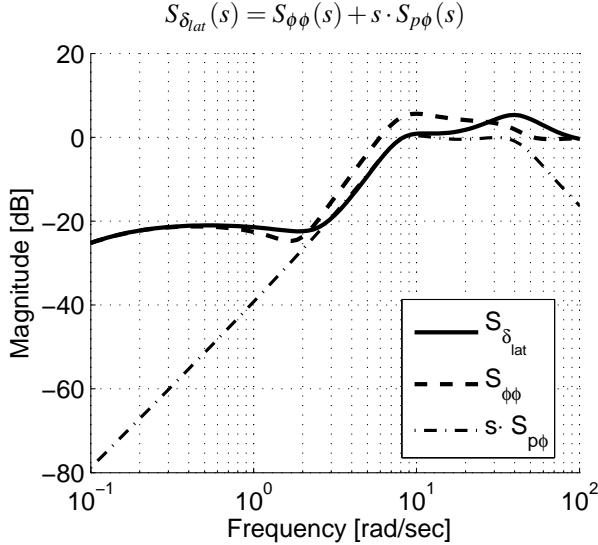


**Fig. 2. Typical shape of an input sensitivity function.**

A similar analysis can be performed for a position feedback block diagram to determine the lateral position error  $y_e$  due to a process disturbance by augmenting the attitude feedback loop with a position hold controller  $\mathbf{K}_y$ , as shown in Figure 3.

For an input disturbance  $\delta_d$  and lateral gust  $v_g$ , the error  $y_e$  is given by:

$$\mathbf{y}_e = -\mathbf{S}_y \mathbf{S}_\phi \mathbf{G}_y \cdot (\mathbf{G}_{\delta_{\text{lat}}}^\phi \cdot D(s) \cdot \delta_d + \mathbf{G}_{v_g}^\phi \cdot v_g) \quad (8)$$

where  $\mathbf{S}_y$  is the matrix of position outer-loop sensitivity functions:

$$\mathbf{S}_y = (\mathbf{I} + \mathbf{G}_y \mathbf{T}_\phi \mathbf{K}_y)^{-1} = \begin{bmatrix} S_{yy}(s) & S_{vy}(s) \\ S_{yv}(s) & S_{vv}(s) \end{bmatrix} \quad (9)$$

and  $\mathbf{T}_\phi$  is the matrix of inner-loop closed-loop responses:

$$\mathbf{T}_\phi = (\mathbf{I} + \mathbf{G}_{\delta_{\text{lat}}}^\phi \mathbf{K}_\phi)^{-1} \mathbf{G}_{\delta_{\text{lat}}}^\phi \mathbf{K}_\phi \mathbf{P}_\phi \quad (10)$$

The position and velocity output sensitivity functions  $S_{yy}$  and  $S_{vv}$ , are also referred to as the lateral position and lateral velocity disturbance rejection frequency responses, respectively (Ref. 10). These responses correspond to the lateral position and velocity outputs due to a lateral position and lateral velocity disturbance at the sensor measurement:

$$S_{yy}(s) = \frac{y'}{y_d}(s) \quad (11)$$

$$S_{vv}(s) = \frac{v'_y}{v_d}(s) \quad (12)$$

The position error  $y_e$  can in turn be expressed as:

$$\mathbf{y}_e = -(S_{yy}(s) + s \cdot S_{vy}(s)) \cdot (S_{\phi\phi}(s) + s \cdot S_{p\phi}(s)) \cdot \left(\frac{y}{\delta_{\text{lat}}}(s) \cdot D(s) \cdot \delta_d + \frac{y}{v_g}(s) \cdot v_g\right) \quad (13)$$

where the expression  $(S_{yy} + s \cdot S_{vy})$  is the input sensitivity transfer function of the outer-loop:

$$S_{\phi_{\text{ref}}}(s) \triangleq \frac{\phi_{\text{ref}}}{\delta_{\text{att}}}(s) = (S_{yy}(s) + s \cdot S_{vy}(s)) \quad (14)$$

Further simplification of Equation 13 yields:

$$\mathbf{y}_e = -S_{\phi_{\text{ref}}}(s) \cdot S_{\delta_{\text{lat}}}(s) \cdot \left(\frac{y}{\delta_{\text{lat}}}(s) \cdot D(s) \cdot \delta_d + \frac{y}{v_g}(s) \cdot v_g\right) \quad (15)$$

The position response to an input disturbance and gust is directly proportional to both the outer-loop input sensitivity  $S_{\phi_{\text{ref}}}(s)$  and the input sensitivity of the inner-loop  $S_{\delta_{\text{lat}}}(s)$  *without* position hold augmentation. This result validates the nested loop optimization strategy (Ref. 7) (Ref. 8). In this strategy, the attitude loop feedback controller is optimized first. Once optimized, the resulting attitude loop controller gains are fixed and then the velocity/position outer-loop feedback controllers are optimized.

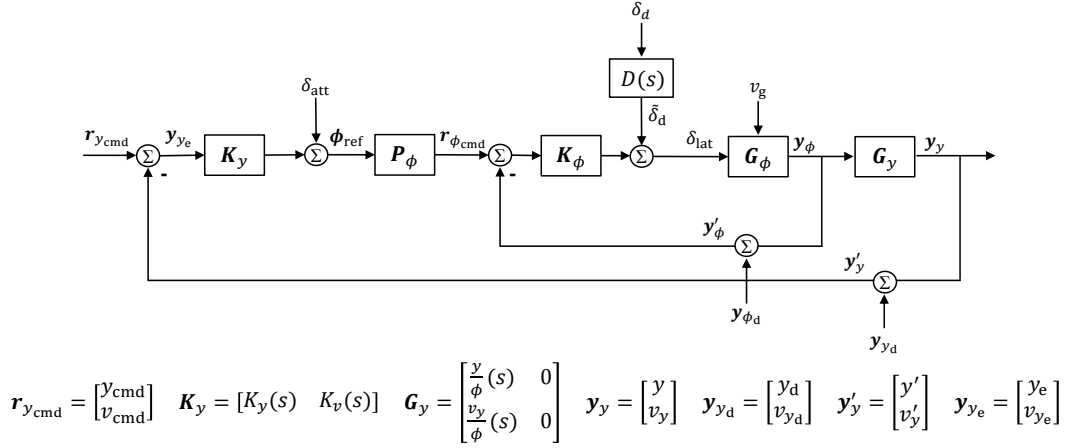


Fig. 3. Lateral-axis position hold control system block diagram.

Furthermore, Equation 15 implies that an aircraft's position hold disturbance rejection performance is directly affected by the aircraft's attitude disturbance rejection characteristics. Knowing the frequency content of the disturbance  $D(s)$  and the aircraft dynamics (e.g.,  $\phi/\delta_{lat}(s)$ ,  $\phi/v_g(s)$ , etc.) provides insight into how each controller  $\mathbf{K}_y$  and  $\mathbf{K}_\phi$  should be designed to attenuate applicable frequencies and produce improved disturbance rejection performance.

### AIRCRAFT DESCRIPTION

The small-scale UAS used in this study is the IRIS+ quadrotor manufactured and sold by 3D Robotics (3DR) (Figure 4). The IRIS+ weighs approximately 2.8 lbs, is 0.3 ft tall, and has a cross motor-to-motor distance of 1.8 ft.



Fig. 4. IRIS+ quadrotor by 3D Robotics.

### Identified Model

A linear state-space model of the IRIS+ around the hover flight condition was identified from flight test data using frequency domain system identification techniques (Ref. 11). The model was then validated in the time domain with pulse responses not used for system identification, ensuring that an accurate model was used for control law design. Due to the quadrotor's symmetric configuration, decoupled lateral, longitudinal, directional, and heave models were identified and then combined into a complete six degree-of-freedom

model. Example identification results are shown here are for the lateral axis only, but similar results were obtained for the other axes.

The form of the identified lateral axis model is given by:

$$\begin{bmatrix} \dot{v} \\ \dot{p} \\ \dot{\phi} \\ \dot{\delta}'_{lat} \end{bmatrix} = \begin{bmatrix} Y_v & Y_p + W_0 & g \cos \Theta_0 & Y_{\delta_{lat}} \\ L_v & L_p & 0 & L_{\delta_{lat}} \\ 0 & 1 & 0 & 0 \\ 0 & 0 & 0 & -1/\tau_{lag} \end{bmatrix} \begin{bmatrix} v - v_g \\ p \\ \phi \\ \delta'_{lat} \end{bmatrix} + \begin{bmatrix} 0 \\ 0 \\ 0 \\ 1/\tau_{lag} \end{bmatrix} \delta_{lat}(t - \tau)$$

$$\begin{bmatrix} p \\ a_y \\ \dot{v} \end{bmatrix} = \begin{bmatrix} 0 & 1 & 0 & 0 \\ Y_v & Y_p & 0 & Y_{\delta_{lat}} \\ Y_v & Y_p + W_0 & g \cos \Theta_0 & Y_{\delta_{lat}} \end{bmatrix} \begin{bmatrix} v \\ p \\ \phi \\ \delta'_{lat} \end{bmatrix} + \begin{bmatrix} 0 \\ 1/\tau_{lag} \\ 1/\tau_{lag} \end{bmatrix} [\delta_{lat}(t - \tau)]$$

(16)

The individual and average frequency response fit cost values are given in Table 1. The costs are calculated as a weighted sum of the magnitude and phase errors between the frequency responses from flight data and the model responses (Ref. 11).

**Table 1. State-Space Model Identification Fit Costs**

Response	Cost ( $J$ )
$p/\delta_{\text{lat}}$	63.36
$a_y/\delta_{\text{lat}}$	24.52
$\dot{v}/\delta_{\text{lat}}$	71.05
$J_{\text{ave}}$	52.98

Figure 5 shows an overlay between flight data (black) and the identified model (blue) for the roll rate to lateral input frequency response of the bare-airframe. The figure shows an excellent model fit, which is confirmed by the low individual and average fit costs given in Table 1 (for rotorcraft, costs of  $J < 100$  indicate an excellent agreement (Ref. 11)).

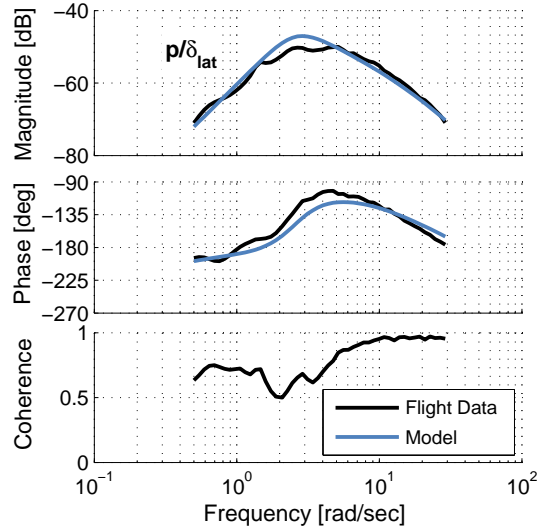


**Fig. 5. Roll rate to lateral input, bare-airframe frequency response. Flight data is in black and the identified model in blue.**

The identified parameter values as well as their insensitivity and Cramér-Rao bounds are given in Table 2. All identified parameters are *known to good accuracy* and not correlated with any other parameters as indicated by their low insensitivity ( $\bar{I} \leq 10\%$  (Ref. 11)) and Cramér-Rao bound ( $\overline{\text{CR}} \leq 20\%$  (Ref. 11)) values.

**Table 2. State-Space Model Identification Parameter Values**

Param.	Value	CR (%)	Insens. (%)
<i>A-matrix</i>			
$Y_v$	-0.1996	6.62	2.37
$Y_p$	0 <sup>a</sup>	—	—
$L_v$	-0.5363	5.78	1.77
$L_p$	0 <sup>a</sup>	—	—
$1/\tau_{\text{lag}}$	19.18 <sup>b</sup>	—	—
<i>B-matrix</i>			
$Y_{\delta_{\text{lat}}}$	0.128	6.62	3.09
$L_{\delta_{\text{lat}}}$	1.601	3.46	1.21
<i>Time delay</i>			
$\tau$	0.0122	13.83	8.132

<sup>a</sup> Eliminated parameter  
<sup>b</sup> Fixed parameter

After identification of the lateral model, it was validated in the time-domain using a verification maneuver consisting of a pulse. The roll rate results are shown in Figure 6, which shows good agreement between flight data and the flight identified model.

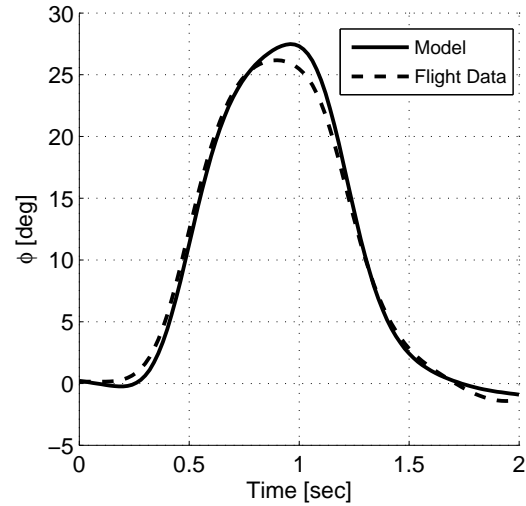


**Fig. 6. Time domain verification of the identified model for a lateral pulse input.**

An alternate model of the IRIS+ was identified and presented in (Ref. 12) and (Ref. 13).

### Comparison to Manned-Sized Helicopter

Useful insight can be gained by comparing the dynamics of the IRIS+ to those of a manned-sized aircraft since

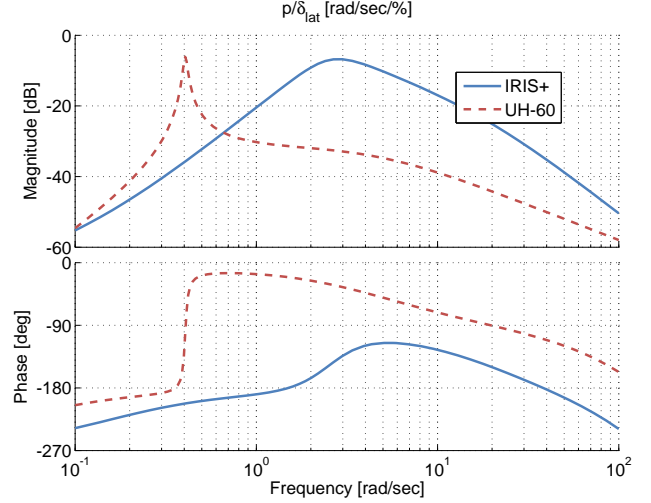
established control law optimization strategies and rules-of-thumb were developed for manned-sized helicopters. Adapting the optimization strategies, rules-of-thumb, and typical control system performance values depends on the dynamics of the bare-airframe.

Table 3 shows a comparison of the primary lateral axis stability and control derivatives between the IRIS+ and a UH-60 (FORECAST hover model used), as well as a comparison of their modes. Two important distinctions can be drawn between the IRIS+ dynamics and those of the UH-60. First, as expected for a much smaller vehicle, the dynamics of the IRIS+ are at a much higher frequency. The IRIS+ unstable lateral phugoid mode has a frequency of  $\omega_{ph_{IRIS+}} = 2.55$  rad/sec, as compared to the UH-60 unstable phugoid value of  $\omega_{ph_{UH-60}} = 0.405$  rad/sec. Using the rule-of-thumb that in order to stabilize an unstable mode, a control system must have a crossover frequency of  $\omega_c \geq 3$  to  $5 \times \omega_{unstable}$  (Ref. 8), we expect typical crossover frequency values of  $\omega_c \geq 13.0$  rad/sec for the IRIS+, whereas typical values for the UH-60 are  $\omega_c \geq 2.0$  rad/sec. An initial estimate of the crossover frequency is a critical characteristic to know before designing a new control system.

The second distinction between the IRIS+ and the UH-60 is the lack of angular rate damping of the IRIS+, as is evident by the values of  $Y_p = 0$  and  $L_p = 0$  (Table 3). The result of this is the lower value of the roll mode frequency ( $1/\tau_r$ ) of the IRIS+, as shown also in Table 3. Figure 7 shows a comparison of the roll rate response of the IRIS+ and UH-60. The lower roll mode frequency of the IRIS+, due to its lack of angular rate damping, results in a reduction in the phase of the roll rate response of about  $\Delta\Phi \approx -60$  deg above  $\omega = 5$  rad/sec, which is a primary reason for the addition of a lead compensator in the control system designed for the IRIS+, as will be discussed later.

**Table 3. Stability and Control Derivative and Mode Comparison Between IRIS+ and UH-60)**

Param.	IRIS+	UH-60
<i>A-matrix</i>		
$Y_v$ [1/sec]	-0.1996	-0.0544
$Y_p$ [ft/rad-sec]	0	0.2897
$L_v$ [rad/ft-sec]	-0.5363	-0.0248
$L_p$ [1/sec]	0	-4.8016
<i>B-matrix</i>		
$Y_{\delta_{lat}}$ [ft/sec <sup>2</sup> /%	0.128	0.0462
$L_{\delta_{lat}}$ [rad/sec <sup>2</sup> /%	1.601	0.1265
<i>Modes</i>		
Phugoid $\omega_{ph}$ [rad/sec]	2.55	0.405
Phugoid $\zeta_{ph}$ [-]	-0.481	-0.0265
Roll $1/\tau_r$ [rad/sec]	2.65	4.83



**Fig. 7. Roll rate frequency response comparison between IRIS+ and UH-60.**

### Turbulence Model

In addition to the bare-airframe model of the IRIS+, a Control Equivalent Turbulence Input (CETI) model (Ref. 14) was developed from flight test data (Ref. 12). The CETI model provides the ability to evaluate the response of the IRIS+ to realistic turbulence and predict the control system performance in terms of RMS attitude or position variations. Attitude and position variations in turbulence are key performance parameters, and therefore enforcing limits on them during control system optimization is a direct method of ensuring they are met. Therefore, having a way to accurately estimate them is necessary.

Like other turbulence models (e.g., Dryden (Ref. 9)), the CETI model is comprised of white noise passed through a low-pass filter. In this case, the filter is first-order:

$$\frac{\delta_{turb}}{wn}(s) = \frac{K}{(s+a)} \quad (17)$$

where  $\delta_{turb}$  is the control equivalent turbulence input, given in percent of the maximum control input, and  $wn$  is white noise with noise power of 1.0.

Table 4 lists the CETI model parameters (gain  $K$  and break frequency  $a$ ) for the IRIS+ and UH-60 medium turbulence CETI models (Ref. 14). Figure 8 shows a comparison of the frequency responses of the two CETI models. Although the CETI model of the IRIS+ has a lower break frequency than that of the UH-60, the steady-state magnitude is higher, as expected for a significantly smaller vehicle that is more susceptible to turbulence.

**Table 4. Control Equivalent Turbulence Input (CETI) Model Comparison Between IRIS+ and UH-60**

Param.	IRIS+	UH-60
$K$ [%]	2.64	1.49
$a$ [rad/sec]	0.351	1.05

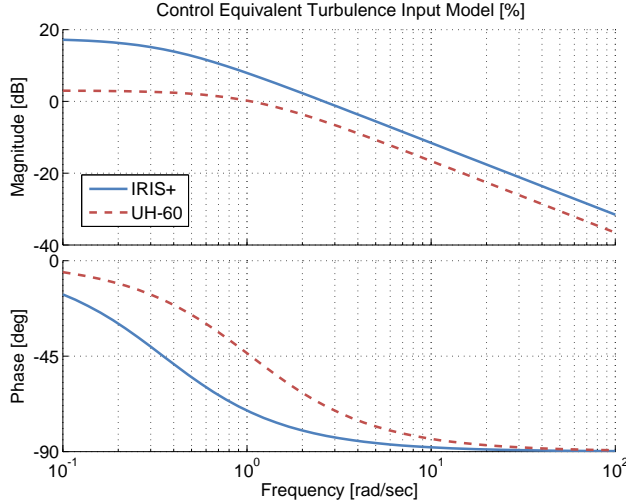


**Fig. 8. Control Equivalent Turbulence Input (CETI) model frequency response comparison between IRIS+ and UH-60.**

## FLIGHT CONTROL DESIGN

A control system was designed for the IRIS+ with the objective of aggressively holding a position over the ground in the presence of wind gusts and turbulence.

Figure 9 shows the block diagram representation of the lateral and longitudinal-axis control system. The controller is comprised of an attitude-command/attitude-hold (ACAH) inner-loop that uses an explicit model following architecture and a simpler position hold (PH) outer-loop feedback controller.

A nested-loop design approach is used where first the ACAH inner-loop is designed for the pitch and roll axes to meet a comprehensive set of stability and performance-based disturbance rejection specifications while minimizing actuator activity. Next, the pitch and roll ACAH designs are fixed augmented with the PH controller. The PH controller is similarly designed to meet a set of design specifications. A direct optimization approach within CONDUIT<sup>®</sup> was used to tune the controller gains (Ref. 8).

### Performance-based Disturbance Rejection

The objective of aggressively holding a position over the ground was accomplished by incorporating performance-

based disturbance rejection requirements directly into the design process. For the purposes of this research, the incorporated performance-based specifications consisted of imposing a minimum performance requirement on the aircraft's disturbance rejection response to CETI turbulence and a 17 ft/sec (10 kt) 1-cosine gust.

**Control Equivalent Turbulence Input (CETI)** As indicated in "Turbulence Modeling" section, the CETI disturbance used herein is generated by passing white noise through a low-pass filter:

$$\text{CETI}(s) = \frac{\delta_{\text{turb}}(s)}{\text{wn}}(s) = k \cdot \frac{2.64}{s + 0.351} \quad (18)$$

where  $k = 100$  PWM/%. In the "Disturbance Rejection" section, it was shown that the roll attitude response to a process disturbance is given by,

$$\frac{\phi}{\delta_d}(s) = S_{\delta_{\text{lat}}}(s) \cdot \frac{\phi}{\delta_{\text{lat}}}(s) \cdot D(s) \quad (19)$$

where the disturbance transfer function  $D(s)$  is now  $\text{CETI}(s)$ . Multiplying the bare-airframe dynamics,  $\phi/\delta_{\text{lat}}(s)$ , with  $\text{CETI}(s)$  produces the open-loop response of the aircraft to CETI turbulence and is shown in Figure 10. Figure 10 shows that 99% of the total energy in the attitude response of the IRIS+ when subjected to CETI turbulence lies between 0.1 - 5 rad/sec. Therefore, feedback control that provides maximum attenuation within this frequency range will yield improved disturbance rejection characteristics. This response is then attenuated by the input sensitivity function  $S_{\delta_{\text{lat}}}(s)$  to ultimately produce the closed-loop attitude response to turbulence.

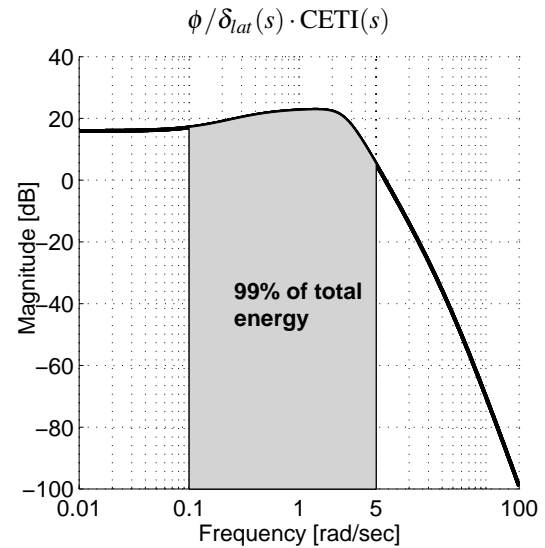


**Fig. 10. Open-loop response of the IRIS+ roll attitude when subjected to CETI turbulence.**

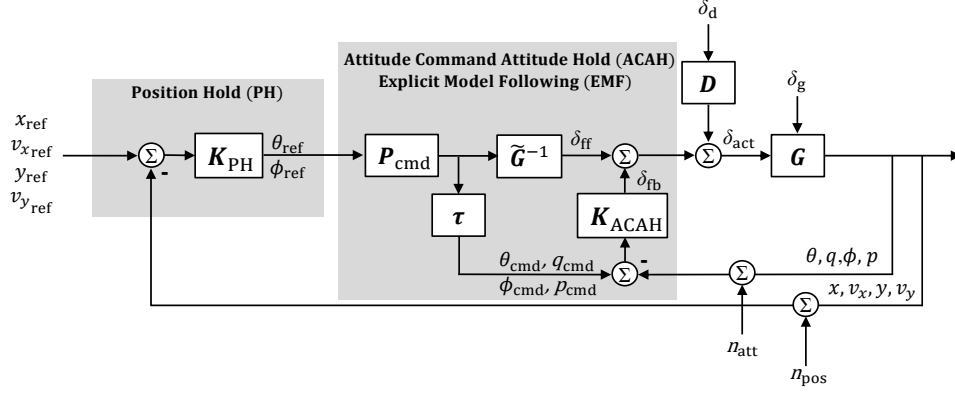


**Fig. 9.** Lateral and longitudinal-axis control system block diagram consisting of an attitude-command/attitude-hold (ACAH) innerloop and position hold (PH) outerloop.

A typical roll attitude error ( $\phi_e$ ) and lateral position error ( $y_e$ ) response of the IRIS+ subjected to CETI turbulence are shown in Figures 11 and 12, respectively. From the response, bounds on the error signal equal to three times the root-mean-square (RMS) are calculated and used as a direct measure of the aircraft's disturbance rejection performance. During the design process, the RMS of the error signal is computed in the frequency domain by calculating the area under the signal's autospectrum (Ref. 8) (Ref. 15). Specific performance requirements (e.g.,  $3\text{-RMS}(\phi_e) \leq 2 \text{ deg}$ ;  $3\text{-RMS}(y_e) \leq 0.5 \text{ ft}$ ) are then imposed and used to drive the flight control design.

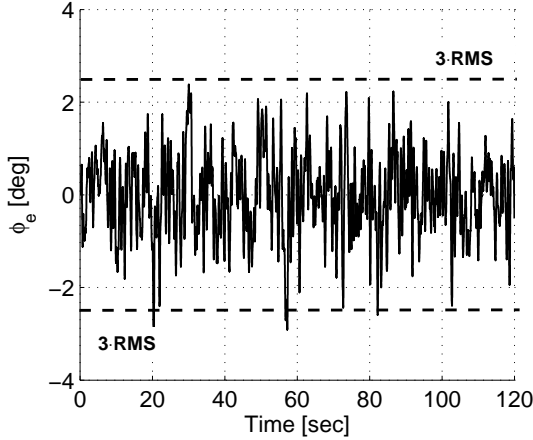


**Fig. 11.** Representative roll attitude error ( $\phi_e$ ) response to CETI turbulence.

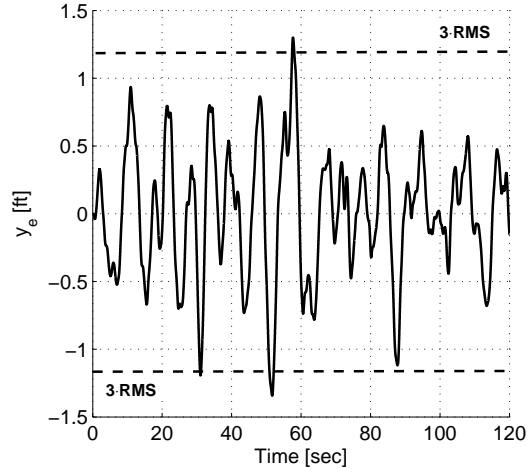


**Fig. 12.** Typical lateral position error ( $y_e$ ) to CETI turbulence.

**1-Cosine Gust Input** A lateral 1-cosine gust input is also used to measure the aircraft's disturbance rejection performance. The lateral gust amplitude,  $v_{\text{gust}}$  is calculated by:

$$v_{\text{gust}} = \frac{v_{\text{max}}}{2}(1 - \cos(\omega_g \cdot t)) \quad (20)$$

where  $v_{\text{max}}$  is the maximum amplitude of the gust and  $\omega_g$  is the frequency of the input. Figure 13 shows the time history profile of an example lateral 17 ft/sec 1-cosine gust.

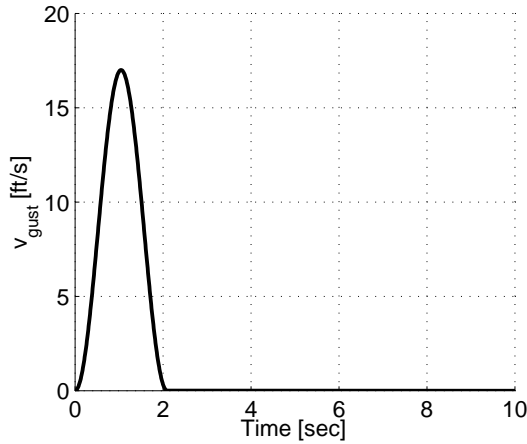


Fig. 13. Representative 1-cosine gust input.

The frequency  $\omega_g$  is dynamically chosen to be the frequency where the maximum magnitude of the gust-to-position ( $y/v_g$ ) frequency response occurs, as shown in Figure 14. The frequency corresponding to the maximum magnitude provides a “worst-case,” or maximum displacement, response for a pure sinusoidal gust input. The 1-cosine input used here is not a continuous sinusoidal signal, however, produces a near maximal displacement response at  $\omega_g$ .

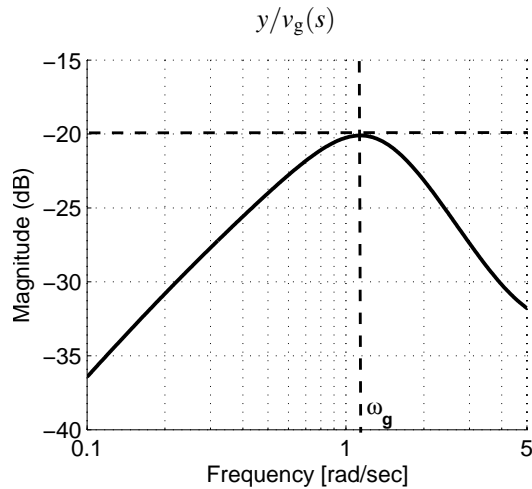


Fig. 14. Representative lateral position frequency response to a gust input.

Figure 15 depicts a typical lateral position response to a 1-cosine  $v_{gust}$ . The maximum displacement of the position response is calculated and used as the disturbance rejection performance measure for the gust input.

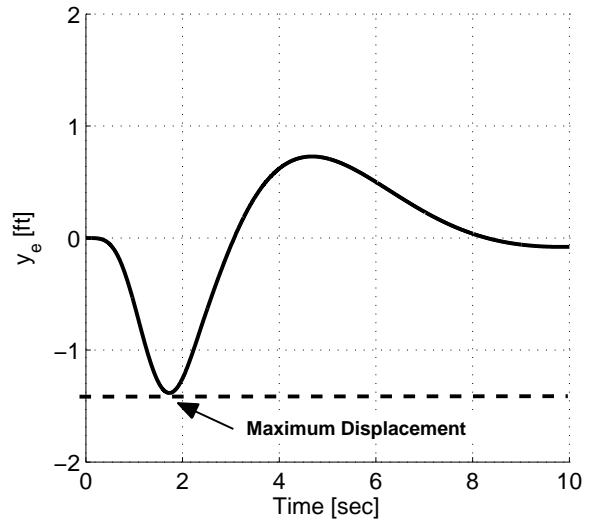


Fig. 15. Representative lateral position response to a 1-cosine gust.

### Attitude Command Attitude Hold (ACAH) Inner-loop Design

The lateral-axis ACAH inner-loop control law is shown in Figure 16 with an identical structure used for the longitudinal axis. Both controllers take the form of an explicit model following (EMF) architecture (Ref. 8). This architecture consists of a command model  $P_\phi$ , inverse plant  $\tilde{G}_\phi^{-1}$ , an equivalent time delay  $\tau_\phi$ , and the feedback controller  $K_\phi$ . An EMF architecture is a two-degree of freedom controller and therefore, allows for the separate design of the inner-loop’s closed loop behavior and the inner-loop’s response to disturbances/modeling uncertainties.

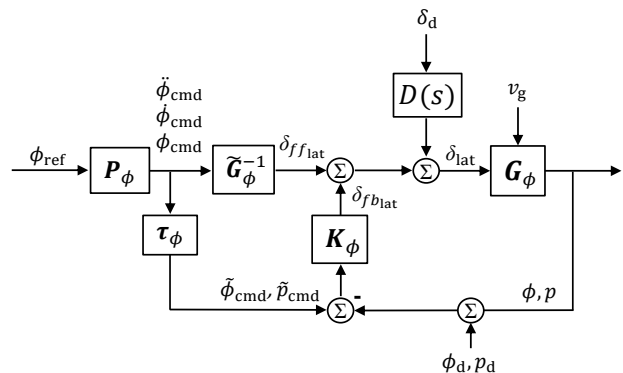


Fig. 16. Lateral-axis ACAH inner-loop control law with an EMF architecture.

The closed-loop response is set by the command model. The command models for both the lateral and longitudinal

axes are second order systems with natural frequency  $\omega_n = 10$  rad/sec and damping ratio  $\zeta = 0.7071$ .

$$P_\phi(s) = P_\theta(s) = \frac{100}{s^2 + 14.1421s + 100} \quad (21)$$

These command model parameters were chosen based on RC pilot preference.

The equivalent time delay is included to account for filtering delays, sampling delays, and high frequency dynamics that are not modeled by the inverse plant. The equivalent time delay for the lateral and longitudinal axis were calculated to be,

$$\tau_\phi = 0.0629 \text{ sec}, \quad \tau_\theta = 0.0657 \text{ sec} \quad (22)$$

Given a commanded attitude, the bare-airframe dynamics are inverted to estimate the required control input necessary to produce said command. For example, the linearized angular acceleration response in the roll axis is given by:

$$\dot{p} = L_v \cdot v + L_{lat} \cdot \delta_{lat} \quad (23)$$

Under the assumption that  $p \approx \dot{\phi}$  and approximating the lateral body velocity to be:

$$v \approx \frac{g}{s - Y_v} \phi \quad (24)$$

the lateral input required to produce a roll attitude command,  $\phi_{cmd}$ , can be estimated by

$$\delta_{fflat} = \frac{\ddot{\phi}_{cmd} - L_v \cdot \frac{g}{s - Y_v} \cdot \phi_{cmd}}{L_{lat}} \quad (25)$$

Similarly, the longitudinal input required to produce a pitch attitude command,  $\theta_{cmd}$ , is estimated by

$$\delta_{fflon} = \frac{\ddot{\theta}_{cmd} - M_u \cdot \frac{-g}{s - X_u} \cdot \theta_{cmd}}{M_{lon}} \quad (26)$$

The lateral axis feedback controller  $K_\phi$  is shown in Figure 17 with an identical structure used in the longitudinal axis. It consists of proportional-integral feedback on roll attitude error ( $\phi_e$ ), proportional feedback on roll rate error ( $p_e$ ), and a lead compensator ( $K_{lead}$ ) such that:

$$K_\phi(s) = \left( \left( \frac{K_{i_\phi}}{s} + K_{p_\phi} \right) \phi_e + K_{p_p} p_e \right) K_{lead}(s) \quad (27)$$

Similarly, for the pitch axis:

$$K_\theta(s) = \left( \left( \frac{K_{i_\theta}}{s} + K_{p_\theta} \right) \theta_e + K_{p_q} q_e \right) K_{lead}(s) \quad (28)$$

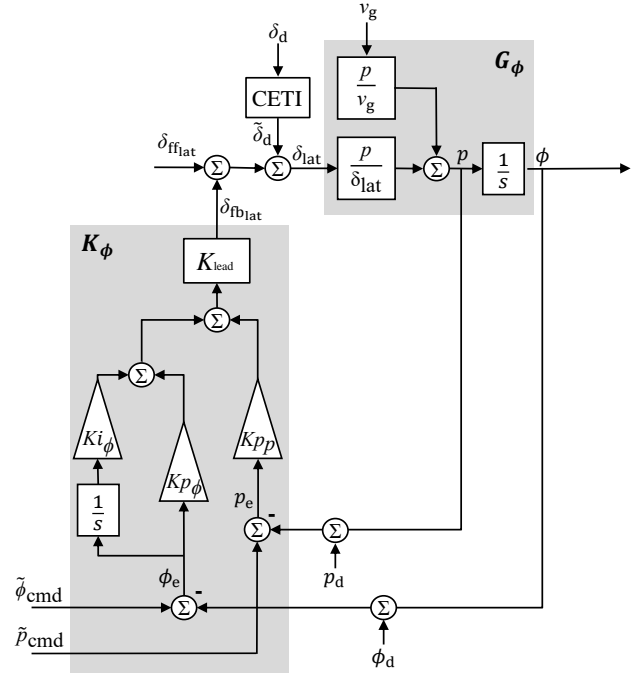


**Fig. 17. Lateral axis feedback control structure.**

The lead compensators were included to account for the reduced phase in the bare-airframe dynamics due to a lack of angular rate damping as described in the ‘‘Aircraft Description’’ section. In addition, it is known that there is a clear trade-off between stability margins and disturbance rejection performance (Ref. 16). Generally, as disturbance rejection performance increases, stability margins decrease. Introducing more phase into the system allows for a larger bandwidth controller with increased disturbance rejection capabilities while still ensuring that pre-defined stability margins are met.

For both the lateral and longitudinal axes, the lead compensator was chosen to provide 80 deg of phase at a nominal crossover frequency of 20 rad/sec. A low-pass filter with break frequency  $\omega = 100$  rad/sec was also included to ensure sufficient roll-off of the control signal at higher frequencies.

**Inner-Loop Flight Control Design Specifications** The feedback gains,  $K_{p_\phi}$ ,  $K_{i_\phi}$ ,  $K_{p_p}$ ,  $K_{p_\theta}$ ,  $K_{i_\theta}$ , and  $K_{p_q}$  were tuned in CONDUIT<sup>®</sup> to simultaneously meet a comprehensive set of stability and performance specifications while minimizing actuator usage. Table 5 summarizes the specifications used for the ACAH control law design and provides

the constraints imposed on each specification. The gain and phase margin requirements in SAE-AS94900 were reduced from their original values.

**Table 5. ACAH Design Specifications**

Description	Source	Constraint
<i>Stability</i>		
Eigenvalues	Generic	L.H.P.
Gain/phase margins	AS94900	[4 dB / 35 deg]
Nichols robust stab. margins	GARTUER	-
<i>Performance</i>		
Eigenvalue damping ratio	Generic	$\geq 0.30$
Crossover frequency	Generic	$\geq 10$ rad/sec
3-RMS Attitude Error - CETI Turbulence	Generic	$\leq [4, 3, 2, 1]$ deg
<i>Actuator Usage</i>		
Actuator RMS - Process noise disturbance	Generic	Minimize

**Inner-Loop Optimization Strategy** The PBDR requirement used to drive the design of the ACAH control system was the 3-RMS attitude error of the aircraft when subjected to CETI turbulence. A family of designs was generated by systematically reducing (tightening) the 3-RMS requirement, for both the roll and pitch axes, from 4 to 1 deg. A 3-RMS of 2 deg was found to be a good compromise between performance and stability and was chosen as the final design. The “UAS Flying Qualities Requirements” presents the results for the entire family of designs.

**Inner-Loop Flight Control Design Results** Figure 18 shows the broken-loop response of the lateral axis with a crossover frequency  $\omega_c = 22.71$  rad/sec, gain margin (GM) of 4.81 dB, and phase margin (PM) of 43.80 deg. The closed-loop response of the lateral axis is also shown in Figure 19 with a -135 degree phase bandwidth of  $\omega_{BW} = 10.61$  rad/sec.

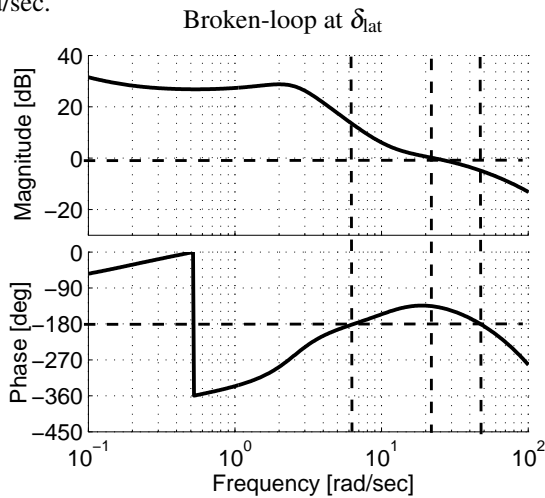


**Fig. 18. Lateral-axis broken-loop response of optimized design.**

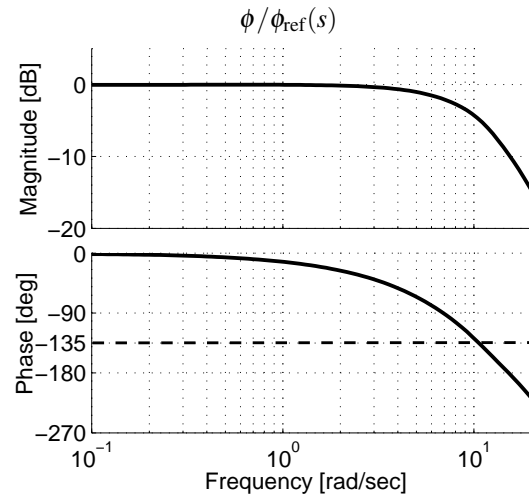


**Fig. 19. Lateral-axis closed-loop response of optimized design.**

Figure 20 shows the lateral axis simulation result of subjecting the IRIS+ to CETI turbulence. The time domain results (3-RMS = 2.1 deg) closely matches the predicted 3-RMS obtained in the frequency domain (3-RMS = 2 deg).

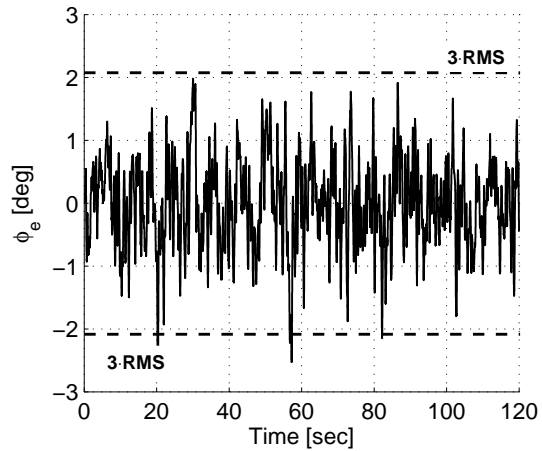


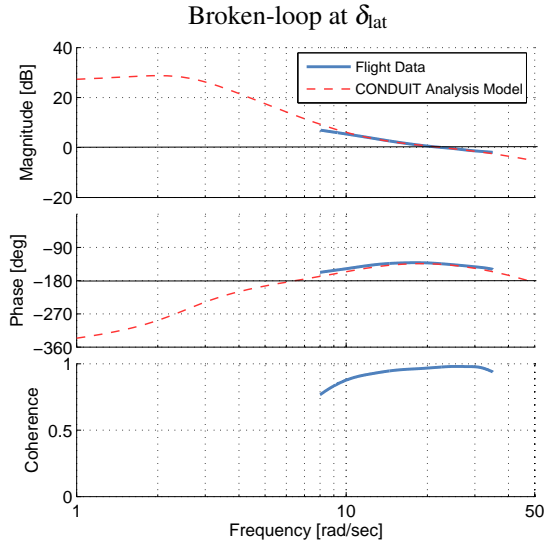
**Fig. 20. Roll attitude error,  $\phi_e$ , of the IRIS+ subjected to CETI turbulence.**

The remaining ACAH design results for a 3-RMS requirement of 2 deg are summarized in Table 6 with all design constraints being met.

**Table 6. ACAH Control Law Design Specification Comparison with Flight Data**

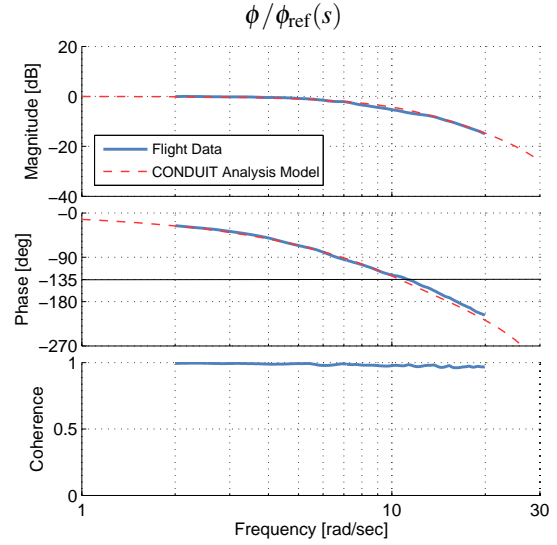
Design	
<i>Roll Axis</i>	
GM [dB]	4.81
PM [deg]	43.80
min( $\zeta$ )	0.30
$\omega_c$ [rad/sec]	22.71
3 · RMS( $\phi_e$ ) [deg]	2.00
$\omega_{BW}$ [rad/sec]	10.61
<i>Pitch Axis</i>	
GM [dB]	4.21
PM [deg]	39.70
min( $\zeta$ )	0.30
$\omega_c$ [rad/sec]	25.24
3 · RMS( $\theta_e$ ) [deg]	2.00
$\omega_{BW}$ [rad/sec]	10.39

**Inner-Loop Design Validation** In order to flight validate the design, broken-loop and closed-loop sweeps of the optimized design were conducted and frequency responses generated using CIPHER<sup>®</sup> (Ref. 11). Figure 21 overlays the lateral broken-loop response obtained from flight data and from the analysis model. Excellent agreement between the two responses is seen around crossover.



**Fig. 21. Broken-loop comparison between flight data and analysis model with optimized design.**

Additionally, the closed loop response obtained from flight data and the analysis model is shown in Figure 22. Excellent agreement is also noted, giving confidence in the accuracy of the analysis model and validity of the implemented design. Similar comparisons between flight data as the analysis model were seen in the pitch axis.



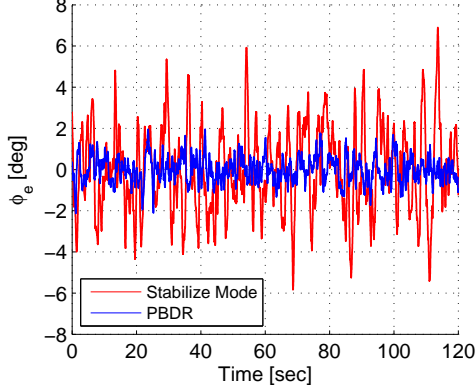
**Fig. 22. Closed-loop response comparison between flight data and analysis model with optimized design.**

Table 7 summarizes the ACAH control law design specifications with those obtained from flight. Excellent agreement is noted in both the lateral and pitch axes.

**Table 7. ACAH Control Law Design Specification Comparison with Flight Data**

	Design	Flight
<i>Roll Axis</i>		
GM [dB]	4.81	-
PM [deg]	43.80	45.50
$\omega_c$ [rad/sec]	22.71	22.67
3 · RMS( $\phi_e$ ) [deg]	2.00	2.03
$\omega_{BW}$ [rad/sec]	10.61	11.25
<i>Pitch Axis</i>		
GM [dB]	4.21	-
PM [deg]	39.70	38.57
$\omega_c$ [rad/sec]	25.24	24.68
3 · RMS( $\theta_e$ ) [deg]	2.00	1.89
$\omega_{BW}$ [rad/sec]	10.39	11.03

**Inner-Loop Flight Test Results** The optimized design and the stock IRIS+ “Stabilize” control systems were flown outdoors with simulated CETI turbulence in 2-3 kt winds. The stock “Stabilize” mode is also an attitude command attitude hold controller. Figure 23 shows the resulting roll attitude error from flight for both the PBDR design and “Stabilize”. A significant improvement can be seen in the performance-based design with a 3-RMS performance measure of 2.03 deg, very close to the predicted/designed value.



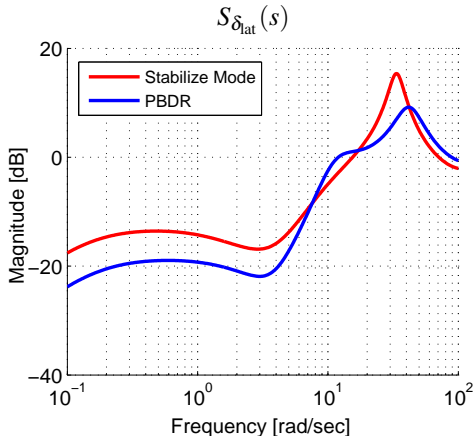
**Fig. 23. Flight data comparison of the roll attitude error between the stock “Stabilize” controller and the performance-based design.**

Table 8 summarizes the pitch and roll 3-RMS attitude error performance measures obtained from flight. For both axes, the measures obtained from flight data match the designed performance measure of 2 deg very closely and are both over a factor of three smaller than the stock controller.

**Table 8. 3-RMS Attitude Error Comparison Between Performance-based Design and Stabilize Mode**

	PBDR [deg]	Stabilize Mode [deg]
3-RMS( $\phi_e$ )	2.03	6.66
3-RMS( $\theta_e$ )	1.89	6.35

**Inner-Loop Discussion** Examining the sensitivity functions for both controllers provides insight into the differences in disturbance rejection characteristics that were observed in flight. Figure 24 shows the lateral axis input sensitivity functions  $S_{\delta_{lat}}$  obtained from analysis for both the PBDR design and the stock controller.



**Fig. 24. Lateral-axis input sensitivity of the performance-based disturbance rejection design and the stock “Stabilize” controller.**

Recall that 99% of the total energy in the attitude response of the IRIS+ due to CETI turbulence lies between 0.1 - 5 rad/sec (Figure 10). This frequency range is the critical region for disturbance rejection and where the sensitivity function is most effective in attenuating this type of disturbance. The PBDR design is roughly 5 dB smaller in magnitude within this entire region, leading to larger disturbance attenuation and an overall smaller 3-RMS attitude error performance measure.

The feedback gain acting on the attitude error that is most effective in shaping the sensitivity function at low frequency is the integrator gain. Proportional-integral feedback can be expressed as:

$$K_p \cdot \frac{s + (K_i/K_p)}{s} \quad (29)$$

where the integrator-to-proportional gain ratio  $K_i/K_p$  is the frequency up to which the integral action is effective. A good rule of thumb is to choose this ratio to be 1/5 of the crossover frequency  $\omega_c$  in order to limit the phase loss/lag at that frequency (Ref. 8) (Ref. 17). With a nominal crossover of  $\omega_c = 20$  rad/sec for the IRIS+, the rule of thumb suggests a ratio of 4. However, significant improvements in disturbance rejection can be obtained by increasing the range of effectiveness of the integrator gain, or equivalently, increasing the integrator-to-proportional gain ratio. This increase in performance comes at a cost of larger phase loss around crossover, further amplifying the need for a lead compensator.

Directly incorporating the 3-RMS attitude error performance measure into the design and optimization process exploited this benefit and produced a controller with significant improvements in disturbance rejection properties. The resulting integrator-to-proportional gain ratio obtained from the optimized design is 13, approximately 3/5 of crossover.

The stock “Stabilize” controller provides lead compensation in the form of derivative action on the angular rate error which allows for a high-bandwidth controller, however, there is no integral action on the attitude error, only a proportional gain.

## PH Outer-loop Design

Using and fixing the feedback gains of the ACAH inner-loop design corresponding to a 3-RMS of 2 deg, position hold (PH) control laws were developed for the lateral and longitudinal axes. The lateral-axis PH outer-loop control law is shown in Figure 25 with an identical structure used in the longitudinal axis. The feedback controller  $K_y$ , consists of proportional-integral feedback on lateral position error ( $y_e$ ), proportional feedback on lateral velocity error ( $v_{y_e}$ ), and a lead compensator ( $K_{y_{lead}}$ ) such that:

$$K_y(s) = \left( \left( \frac{K_{i_y}}{s} + K_{p_y} \right) y_e + K_{p_{v_y}} v_{y_e} \right) \cdot K_{y_{lead}}(s) \quad (30)$$

Similarly, for the pitch axis:

$$K_x(s) = \left( \left( \frac{K_{ix}}{s} + K_{px} \right) x_e + K_{pv_x} v_{x_e} \right) \cdot K_{x_{lead}}(s) \quad (31)$$

As with the ACAH inner-loop design, the lead compensators were included to allow for increased gains while ensuring adequate stability margins were still maintained. For both axes, the lead compensator was chosen to provide 45 deg of phase at a nominal outer-loop crossover frequency of  $\omega_c = 4$  rad/sec. For simplicity, the integrator-to-proportional gain ratio was set to 0.8, 1/5 of the nominal outer-loop crossover frequency of 4 rad/sec.

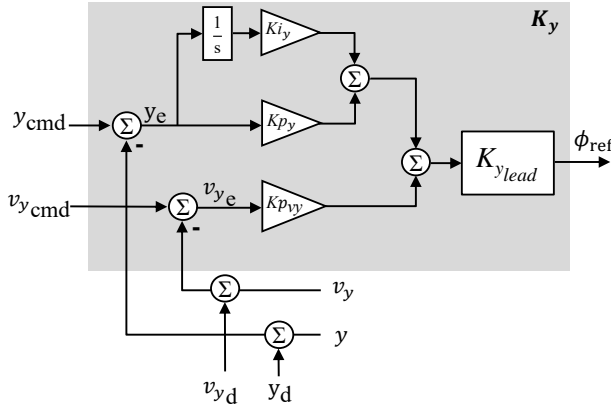


**Fig. 25. Lateral-axis position hold (PH) control law structure.**

**Outer-Loop Flight Control Design Specifications** The feedback gains,  $K_{py}$ ,  $K_{pv_y}$ ,  $K_{px}$ , and  $K_{pv_x}$  were tuned to simultaneously meet a comprehensive set of stability and performance specifications while minimizing actuator usage. Table 9 summarizes the specifications used for the PH control law design and provides the constraints imposed on each specification.

**Table 9. PH Design Specifications**

Description	Source	Constraint
<i>Stability</i>		
Eigenvalues	Generic	L.H.P.
Gain/phase margins	AS94900	[4 dB / 35 deg]
- Inner-loop		
- Outer-loop		
Nichols robust stab. margins	GARTUER	-
- Inner-loop		
- Outer-loop		
<i>Performance</i>		
Eigenvalue damping ratio	Generic	$\geq 0.3$
Crossover frequency	Generic	$\geq 1$ rad/sec
- Outer-loop		
3-RMS Position Error	Generic	$\leq 0.5$ ft
- CETI Turbulence		
Max position displacement	Generic	$\leq 1$ ft
- 10 kt 1-cosine Gust		
<i>Actuator Usage</i>		
Actuator RMS	Generic	Minimize
- Process noise disturbance		

**Outer-Loop Optimization Strategy** The performance-based disturbance rejection requirements used in the design of the PH control system were the 3-RMS position error of the aircraft when subjected to CETI turbulence and the maximum displacement of the aircraft due to a 10 kt 1-cosine gust. A family of designs were generated by systematically reducing the maximum displacement requirement, for both the lateral and longitudinal axes. In both cases, the performance requirement was reduced until further reduction caused a violation in one of the pre-defined design constraints.

**Outer-Loop Flight Control Design Results** During the optimization process, a minimum maximum-displacement to a 1-cosine gust performance measure of 0.37 ft was achieved in the lateral axis, while a minimum performance measure of 0.50 ft was achieved in the longitudinal axis.

Figure 26 shows the lateral-axis broken-loop response, broken at the actuator ( $\delta_{lat}$ ), with a crossover frequency of  $\omega_c = 22.8$  rad/sec, GM of 5.18 dB, and PM of 45 deg. The outer-loop broken-loop response, broken at the roll reference command ( $\phi_{ref}$ ) is shown in Figure 27 and has a crossover frequency of  $\omega_c = 4$  rad/sec, GM of 7.07, and PM of 49.08 deg.

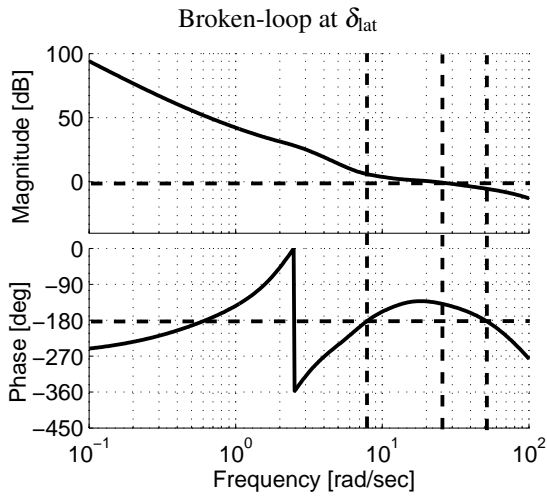


**Fig. 26. Lateral-axis broken loop response (broken at the actuator,  $\delta_{lat}$ ) of the optimized design.**

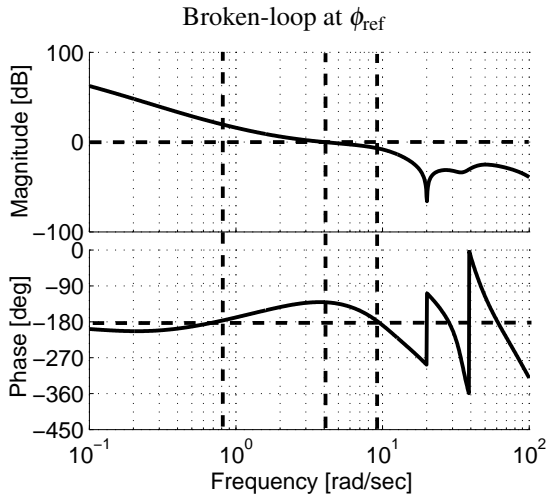


**Fig. 27. Lateral-axis broken loop response (broken at the roll reference command,  $\phi_{ref}$ ) of the optimized design.**

Figure 28 depicts the lateral position response of the vehicle when subjected to CETI turbulence and shows the effectiveness of the PH controller, allowing the aircraft to maintain position within 0.15 ft. In Figure 29, the lateral position response to a 10 kt 1-cosine gust is shown with the vehicle reaching a maximum displacement of the design value 0.37 ft. The remaining lateral and longitudinal PH design results are summarized in Tables 10 and 11, respectively.

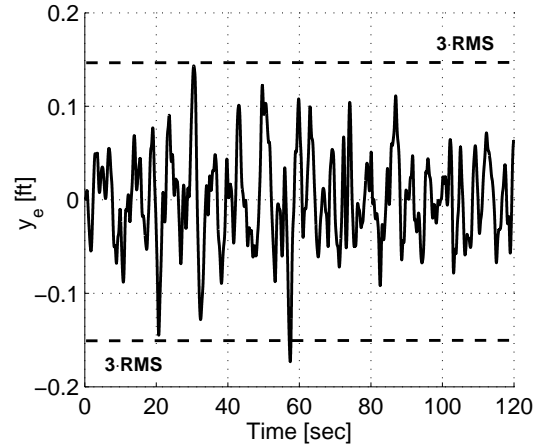


**Fig. 28. Lateral position response to CETI turbulence of the optimized design.**

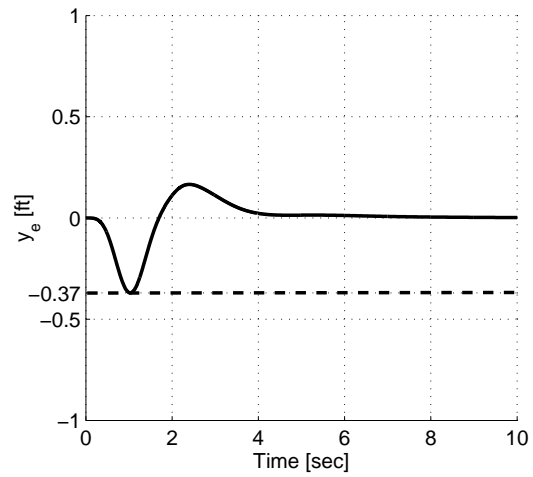


**Fig. 29. Lateral position response to a 10 kt 1-cosine gust of the optimized design.**

**Table 10. Lateral-Axis PH Control Law Design Results**

Lateral-Axis	Design
<i>Attitude Loop</i>	
GM [dB]	5.21
PM [deg]	44.45
$\omega_c$ [rad/sec]	22.97
<i>Position Loop</i>	
GM [dB]	7.07
PM [deg]	49.08
$\omega_c$ [rad/sec]	4.0
$\omega_{BW}$ [rad/sec]	10.13
<i>Performance</i>	
$\min(\zeta)$	0.30
$3 \cdot \text{RMS}(y_e)$ [ft]	0.14
- CETI Turbulence	
Max Displacement [ft]	0.37
- 10 kt 1-cosine Gust	

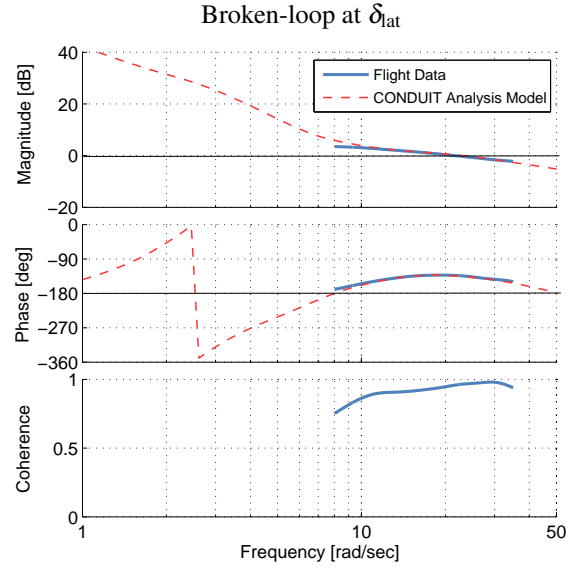


**Fig. 30. Broken-loop comparison between flight data and analysis model with optimized design.**

**Table 11. Longitudinal-Axis PH Control Law Design Results**

Longitudinal-Axis	Design
<i>Attitude Loop</i>	
GM [dB]	4.37
PM [deg]	38.19
$\omega_c$ [rad/sec]	25.31
<i>Position Loop</i>	
GM [dB]	7.12
PM [deg]	69.36
$\omega_c$ [rad/sec]	4.30
$\omega_{BW}$ [rad/sec]	10.90
<i>Performance</i>	
$\min(\zeta)$	0.30
$3 \cdot \text{RMS}(x_e)$ [ft]	0.11
- CETI Turbulence	
Max Displacement [ft]	0.50
- 10 kt 1-cosine Gust	

Additionally, the closed-loop response obtained from flight data and the analysis model is shown in Figure 31. Excellent agreement is noted, validating the analysis model and design implementation. Similar results were noted in the longitudinal axis.

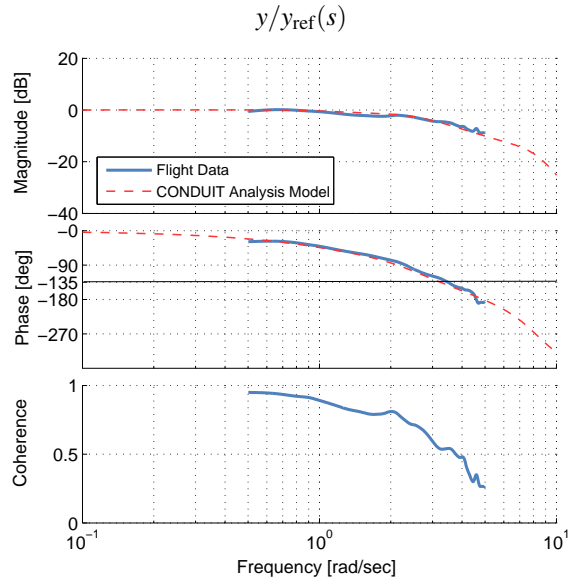


**Fig. 31. Position hold closed-loop response comparison between flight data and analysis model with optimized design.**

**Outer-Loop Design Validation** In order to flight validate the PH design, broken-loop and closed-loop sweeps were performed. Figure 30 shows an overlay of the lateral axis broken-loop response (broken at the actuator/inner-loop) obtained from flight data and from the analysis model used for control law optimization. Again, great agreement between the two responses is seen around crossover.

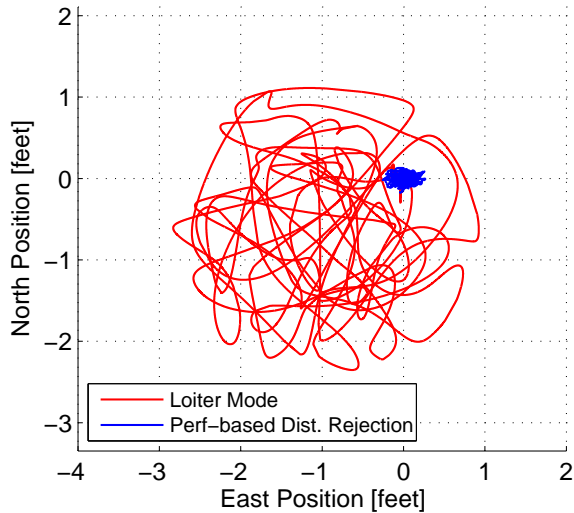
Table 12 summarizes the PH control law design specifications with those obtained from flight, showing excellent agreement and validating the analysis model and implementation of the control laws on the IRIS+.

**Table 12. PH Control Law Design Specification Comparison with Flight Data**

	Design	Flight
<i>Roll Axis</i>		
GM [dB]	5.18	-
PM [deg]	45.00	47.00
$\omega_c$ [rad/sec]	22.8	21.56
Max $y_{gust}$ [ft]	0.37	-
$\omega_{BW}$ [rad/sec]	3.24	3.49
<i>Pitch Axis</i>		
GM [dB]	4.37	-
PM [deg]	38.19	36.73
$\omega_c$ [rad/sec]	25.31	24.68
Max $x_{gust}$ [ft]	0.50	-
$\omega_{BW}$ [rad/sec]	3.33	3.61

**Outer-Loop Flight Test Results** The optimized PH design and the stock IRIS+ “Loiter” PH control system were flown outdoors in 2-3 kts of wind with simulated CETI turbulence. Because 1-cosine gusts could not be recreated in flight, the 3-RMS position error was used to measure the performance of each controller.

Figure 32 shows the resulting position response for both the PBDR design and “Loiter” mode. A significant improvement can be seen in the PBDR design with a 3-RMS position error of 0.28 ft in the lateral axis and 0.14 ft in the longitudinal axis, an order of magnitude improvement over the stock “Loiter” PH controller.



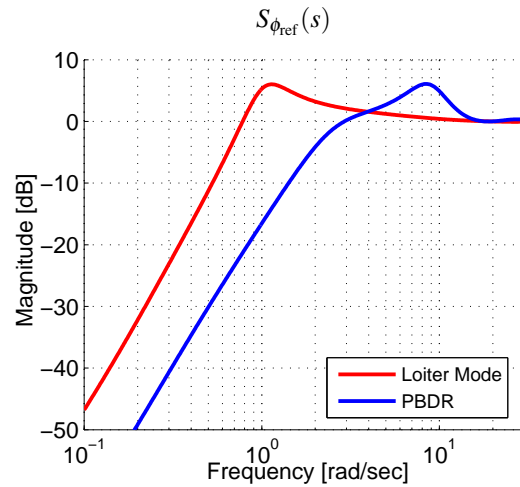
**Fig. 32. Position response from flight data, for both the performance-based disturbance rejection design and stock “Loiter” control system in CETI turbulence.**

Table 13 summarizes the 3-RMS position error obtained from flight for both controllers.

**Table 13. 3-RMS Position Error Comparison Between Performance-based Design and Loiter Mode**

	PBDR [ft]	Loiter Mode [ft]
3· RMS( $y_e$ )	0.28	3.85
3· RMS( $x_e$ )	0.14	3.13

**Outer-Loop Discussion** In the “Disturbance Rejection” section it was shown that the aircraft’s position hold performance is directly proportional to both the input sensitivity ( $S_{\delta_{lat}}$ ), with no PH augmentation, and the sensitivity function of the outer-loop ( $S_{\phi_{ref}}$ ). Figure 33 shows the outer-loop sensitivity function obtained from analysis for both the PH PBDR design and the stock controller.



**Fig. 33. Outer-loop input sensitivity function analysis model for the performance-based disturbance rejection design and stock “Loiter” control system.**

As was the case for the input sensitivity without PH augmentation (Figure 24), the magnitude of the performance-based design is much lower than the stock controller within the critical frequency range for disturbance rejection. The lead compensator used in the PH controller allowed for a design with larger gains, and consequently greater attenuation in the outer-loop sensitivity function, while still meeting imposed stability margin constraints. The combined attenuation between  $S_{\phi_{ref}}$  and  $S_{\delta_{lat}}$  yields the overall disturbance rejection characteristics of the system and is shown in Figure 34.

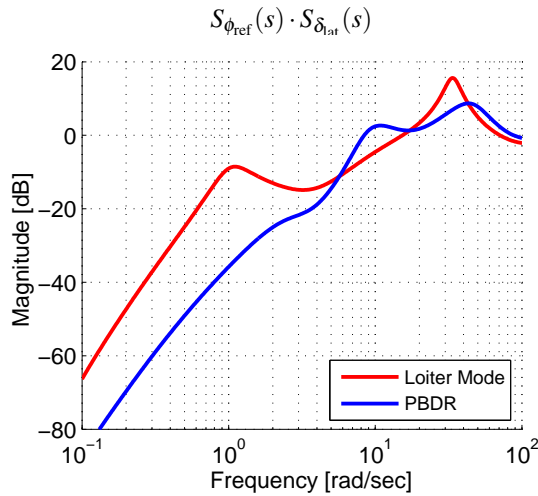


**Fig. 34. Input sensitivity function analysis model for the performance-based disturbance rejection design and stock “Loiter” control system..**

As expected, the overall response of the performance-based PH design is greatly attenuated when compared to the stock control system. From Bode’s Integral Theorem, it is known that any attenuation of the sensitivity function at a given frequency corresponds to an amplification at another frequency (“water-bed effect”) (Ref. 18). Using a performance-based design process allowed the optimization to “transfer” the energy of the sensitivity function from the lower frequencies where turbulence is active to higher frequencies where the magnitude of the IRIS+ bare-airframe dynamics and the disturbance shaping function roll off (Figures 7 - 8).

### UAS FLYING QUALITIES REQUIREMENTS

Using a performance-based design approach, flight control systems with various levels of disturbance rejection characteristics can be developed. The performance of each design can in turn be correlated with existing flying qualities specifications to provide flight control design guidelines for UAS. The suitability of this approach in determining appropriate values for typical flying qualities is examined by using the four ACAH designs developed with increasing levels of performance.

### ACAH Metrics

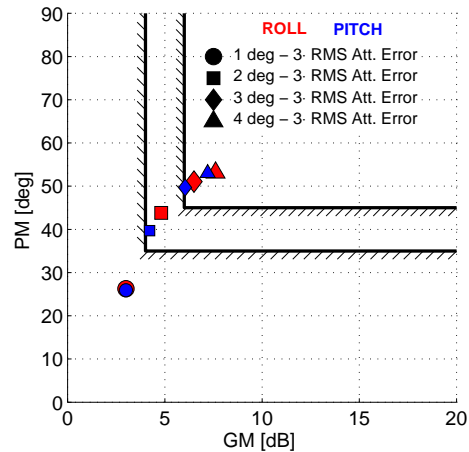
The performance-based requirement used during the ACAH flight control design was the 3-RMS attitude tracking error to CETI turbulence. Designs with constraints of 4, 3, 2, and 1 degree 3-RMS tracking error were developed, flight tested with CETI turbulence, and the corresponding flying qualities metrics were tabulated. Table 8 compares the four designed performance measures with those obtained from flight. The excellent agreement between the designed and

flight values lends validity to the fidelity of the model-based design and to the resulting flying qualities associated with each performance measure.

**Table 14. 3-RMS Attitude Error Comparison With Flight Data**

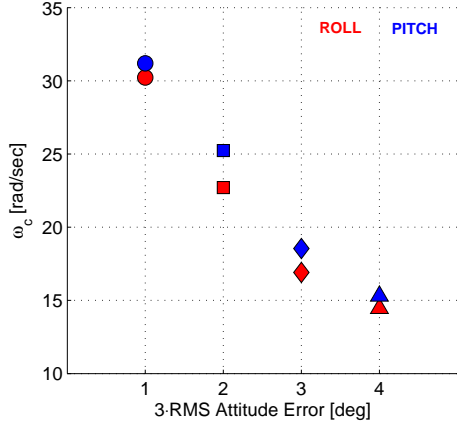
Design [deg]	Flight ( $\phi_{err}$ ) [deg]	Flight ( $\theta_{err}$ ) [deg]
1.00	0.94	1.00
2.00	2.03	1.89
3.00	2.99	3.09
4.00	4.12	3.92

Figure 35 shows the gain and phase margins for the four designs superimposed on the stability margin specification from SAE-AS-94900. As expected, an increase in disturbance rejection performance comes at the cost of reduced stability margins with the most aggressive design having a GM of 3 dB and a PM of 26 deg for both axes.



**Fig. 35. Stability margins for ACAH designs with increasing levels of performance.**

The crossover frequency  $\omega_c$  for each design is shown in Figure 36. A clear trend of increasing crossover frequency for increasing levels of performance is observed with values ranging from 15 rad/sec for the least aggressive design to over 30 rad/sec.



**Fig. 36. Crossover frequency  $\omega_c$  for ACAH designs with increasing levels of performance.**

Figure 37 shows the disturbance rejection bandwidth  $\omega_{DRB}$  for the four designs and Figure 38 the disturbance rejection peak DRP.

The attitude disturbance rejection bandwidth is the frequency where the magnitude of the attitude sensitivity function (e.g.,  $S_{\phi\phi}$  from Equation 5) is -3 dB. The criteria was developed by the Aviation Development Directorate (ADD) for full-scale, UH-60 sized rotorcraft (Ref. 10) and established by correlating numerical values with Level 1 Cooper-Harper handling quality ratings for the hover ADS-33E Mission Task Element flown in turbulence. The attitude disturbance rejection peak is the maximum magnitude of the attitude sensitivity function.

Again, a distinct trend is observed. Increasing disturbance rejection bandwidth results in increased performance. The DRB values obtained are approximately a factor of 10 larger than the current ADS-33 values for full-sized vehicles.

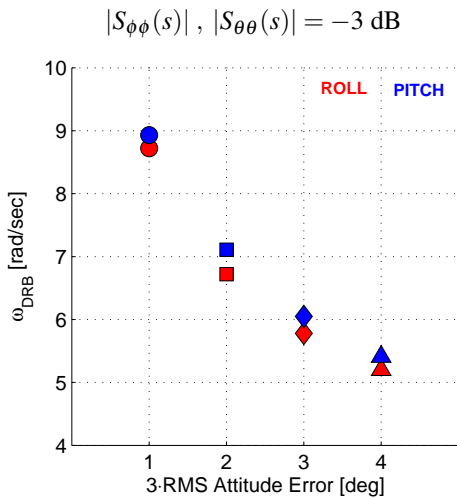


**Fig. 37. Disturbance rejection bandwidth (DRB) for ACAH designs with increasing levels of performance.**

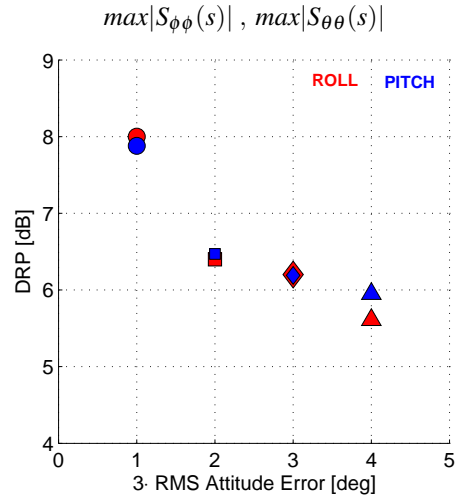


**Fig. 38. Disturbance rejection peak (DRP) for ACAH designs with increasing levels of performance.**

The -3dB bandwidth and peak magnitude of the input sensitivity function  $S_{\delta_{at}}$  has also been used as a disturbance rejection metric and has been referred to as the control equivalent disturbance rejection bandwidth/peak (CDRB/CDRP) (Ref. 19). Figures 39 and 40 show these two metrics. Similar to DRB and DRP, clear trends are seen for the bandwidth and peak of the input sensitivity function.

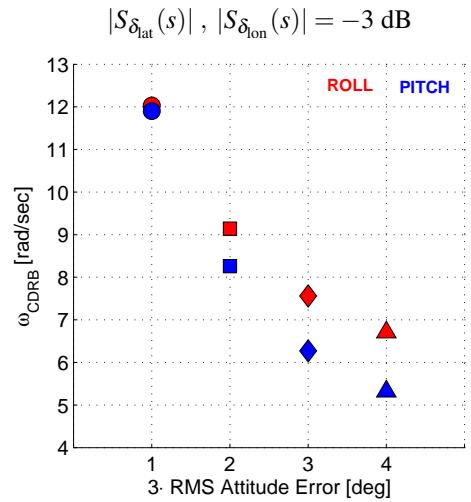


**Fig. 39. Control equivalent disturbance rejection bandwidth (CDRB) for ACAH designs with increasing levels of performance.**

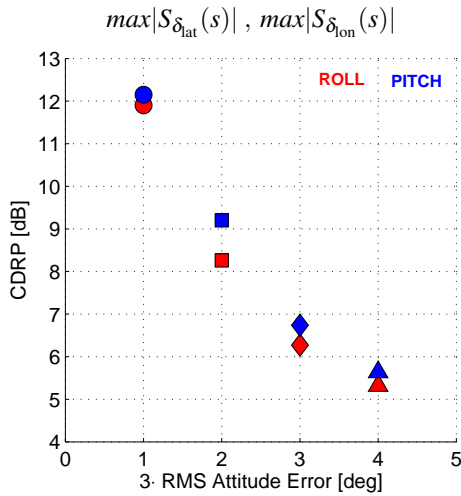


**Fig. 40. Control equivalent disturbance rejection peak (CDRP) for ACAH designs with increasing levels of performance.**

Figure 41 shows the integrator-to-proportional gain ratio in percent of crossover for the 4 designs. For all four designs, a factor of  $\approx 3/5$  of  $\omega_c$  is seen, contrast to the  $1/5$  of  $\omega_c$  rule of thumb.

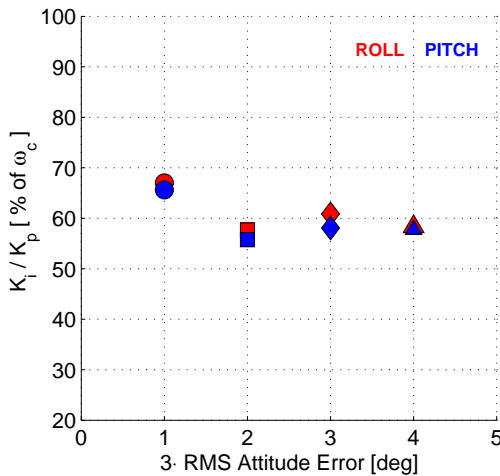


**Fig. 41. Integral-to-proportional gain ratio in percentage of each design's crossover frequency.**

For the metrics shown, clear trends in their correlation with disturbance rejection performance were noted. Each metric alone, however, does not guarantee a certain level of performance and it is important to examine a comprehensive set of specifications. Given a set of specifications that accurately defines the flying qualities of a vehicle, combined with defined performance requirements, a similar performance-based design approach can be used to determine desired flying qualities for UAS.

## PH Metrics

Using the inner-loop design corresponding to a 3-RMS of 2 deg, three outer-loop PH designs were developed with increasing levels of performance. For the lateral axis, designs imposing a maximum 1-cosine gust position displacement of 0.37, 0.5, and 1.0 ft were developed. For the longitudinal axis, performance measures of 0.5 ft, 0.75 ft, and 1.0 ft were used.

The following figures summarize common flying qualities metrics obtained from the three PH designs and are intended to show trends and provide insight into typical values expected for similar type and sized UAS.

The outer-loop position disturbance rejection bandwidth is the frequency where the magnitude of the position sensitivity function (e.g.,  $S_{y,y}$  from Equation 9) is -3 dB. Similarly, the outer-loop control equivalent disturbance rejection bandwidth is the frequency where the magnitude of the outer-loop input sensitivity function  $S_{\phi_{ref}}$  is -3dB.

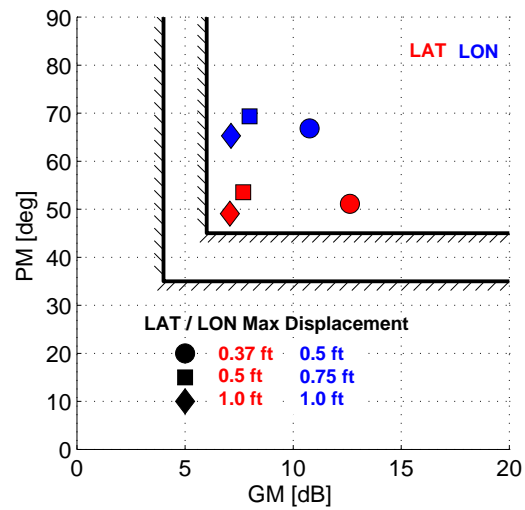


**Fig. 42. Outer-loop stability margins for PH designs with increasing levels of performance.**

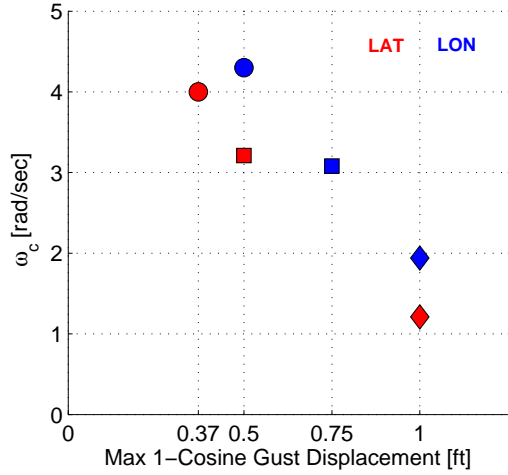


Fig. 43. Outer-loop crossover frequency  $\omega_c$  for PH designs with increasing levels of performance.

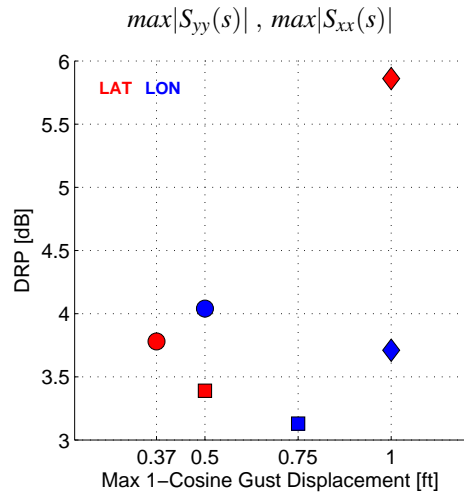


Fig. 45. Outer-loop disturbance rejection peak (DRP) for PH designs with increasing levels of performance.

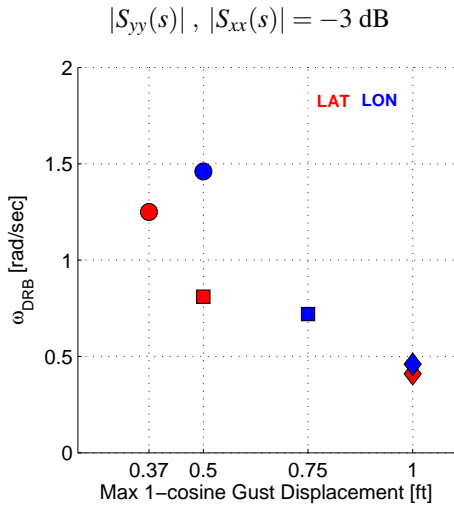


Fig. 44. Outer-loop disturbance rejection bandwidth (DRB) for PH designs with increasing levels of performance.

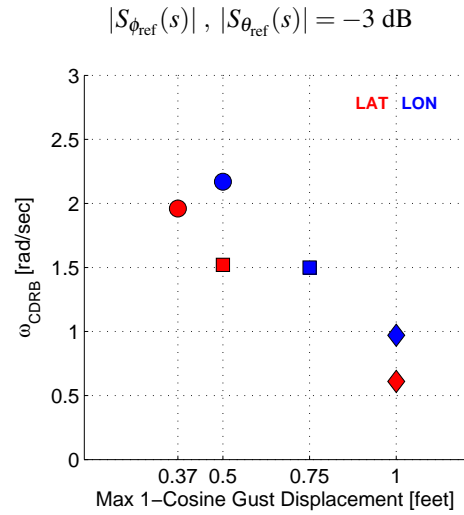
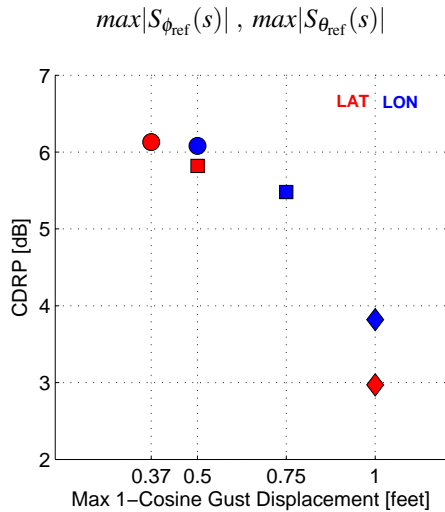


Fig. 46. Outer-loop control equivalent disturbance rejection bandwidth (CDRB) for PH designs with increasing levels of performance.



**Fig. 47. Outer-loop control equivalent disturbance rejection peak (CDRP) for PH designs with increasing levels of performance.**

## CONCLUSION

A flight control system for the IRIS+ quadrotor was designed and flight tested to aggressively hold a position over the ground in the presence of wind gusts and turbulence. The following conclusions were noted:

1. For any control system with sequential loops, the response of the outer-loop variables to a process disturbance depends on the outer-loop sensitivity function and the inner-loop sensitivity function *without* the outer-loop closed. This result was shown here for an aircraft control system consisting of an inner attitude-hold loop and an outer position-hold loop where the position response to input disturbances (e.g., gust and turbulence) is directly proportional to both the input sensitivity function of the outer-loop  $S_{\phi_{ref}}$  and the input sensitivity of the inner-loop  $S_{\delta_{lat}}(s)$  *without* position hold augmentation. Consequently, an aircraft's position hold performance is a function of its attitude disturbance rejection characteristics.
2. In order to design a high bandwidth controller for the IRIS+ quadrotor with acceptable disturbance rejection performance, lead compensation is needed to provide additional phase around crossover due to a lack of angular rate damping in the bare-airframe dynamics.
3. Excellent validation between the analysis model and flight data was seen in closed/broken-loop frequency response overlays as well as in the comparison of the 3-RMS attitude/position tracking error in turbulence. This result highlights the importance of accurate bare-airframe and turbulence models for use in the

performance-based design process described in this paper. When an accurate turbulence model is not available, values of typical attitude and position hold metrics (e.g., disturbance rejection bandwidth and peak) were provided as a guideline. Typical flight control and flying qualities metrics were observed to be roughly an order of magnitude greater than those for manned-sized aircraft (e.g., UH-60).

4. The critical frequency range for disturbance rejection performance due to Control Equivalent Turbulence Input (CETI) turbulence is 0.1 - 5 rad/sec for the IRIS+ quadrotor. To maximize disturbance attenuation within this frequency range, an integrator-to-proportional gain ratio of  $\approx 3/5$  of the crossover frequency  $\omega_c$  is suggested.
5. Incorporating performance-based disturbance rejection (PBDR) requirements directly into the flight control design process allowed for the development of a position hold controller for the IRIS+ quadrotor with significantly improved disturbance rejection characteristics over the stock control system. The quadrotor was able to hold its position to within 3.5 inches with the PBDR design, a factor of 13.5 improvement over the stock position hold controller.

## ACKNOWLEDGMENTS

The authors would like to thank Mark J.S. Lopez, Eric L. Tobias, and Joseph A. Wagster IV for serving as safety observers, ground control station managers, and test leads during the execution of the outdoor flight experiments.

## REFERENCES

- <sup>1</sup>Hoffmann, G. M., Waslander, S. L., and Tomlin, C. J., "Quadrotor Helicopter Trajectory Tracking Control," presented at the AIAA Guidance, Navigation, and Control Conference and Exhibit, Honolulu, HI, 2008.
- <sup>2</sup>Sahul, M. P. V., Chander, N. V., and Kurian, T., "A Novel Method on Disturbance Rejection PID Controller for Quadcopter Based on Optimization Algorithm," presented at the Third International Conference on Advances in Control and Optimization of Dynamical Systems, Kanpur, India, 2014.
- <sup>3</sup>Waslander, S. L. and Wang, C., "Wind Disturbance Estimation and Rejection for Quadrotor Position Control," presented at the AIAA Information Control, Aerospace Conference, Seattle, WA, 2009.
- <sup>4</sup>Horn, J. F., Sparbanie, S., Cooper, J., and Schierman, J., "Adaptive Gust Alleviation for a Tilt-Rotor UAV operating in Turbulent Airwakes," presented at the AIAA Guidance, Navigation, and Control Conference and Exhibit, Honolulu, HI, 2008.

<sup>5</sup>Tischler, M. B., *Advances in Aircraft Flight Control*, Taylor and Francis, 1996.

<sup>6</sup>Lee, D. and Horn, J. F., "Optimization of a Helicopter Stability Augmentation System for Operation in a Ship Airwake," presented at the American Helicopter Society 61st Annual Forum, Grapevine, TX, 2005.

<sup>7</sup>Mansur, M. H. and Tischler, M. B., "Flight Test Comparison of Alternate Strategies for Multi-Loop Control Law Optimization," presented at the American Helicopter Society 69th Annual Forum, Phoenix, AZ, 2013.

<sup>8</sup>Tischler, M. B., Berger, T., Ivler, C. M., Mansur, H., Mohammadreza, Cheung, K. K., and Soong, J. Y., *Practical Methods for Aircraft and Rotorcraft Flight Control Design: An Optimization Based Approach*, AIAA, 2017.

<sup>9</sup>Anon., "Flying Qualities of Piloted Aircraft," MIL-STD-1797B, Department of Defense Interface Standard, 2006.

<sup>10</sup>Berger, T., Ivler, C. M., Berrios, M. G., and Tischler, M. B., "Disturbance Rejection Handling Qualities Criteria for Rotorcraft," presented at the American Helicopter Society 72nd Annual Forum, West Palm Beach, FL, 2016.

<sup>11</sup>Tischler, M. B. and Remple, R. K., *Aircraft and Rotorcraft System Identification: Engineering Methods and Flight Test Examples Second Edition*, AIAA, 2012.

<sup>12</sup>Juhasz, O., Lopez, M. J., Berrios, M. G., Berger, T., and Tischler, M. B., "Turbulence Modeling of a Small Quadrotor UAS Using System Identification from Flight Data," presented at the Seventh AHS Technical Meeting on VTOL Unmanned Aircraft Systems, Mesa, AZ, 2017.

<sup>13</sup>Cheung, K. K. and et al., "An Overview of the U.S. Army Aviation Development Directorate Quadrotor Guidance, Navigation, and Control Project," presented at the 73rd American Helicopter Society Annual Forum, Fort Worth, TX, 2017.

<sup>14</sup>Lusardi, J. A., von Gruenhagen, W., and Seher-Weiss, S., "Parametric Turbulence Modelling for Rotorcraft Applications, Approach, Flight Tests and Verification," presented at the Rotorcraft Handling Qualities Conference, University of Liverpool, UK, 2008.

<sup>15</sup>Mansur, M. H., Lusardi, J. A., Tischler, M. B., and Berger, T., "Achieving the Best Compromise between Stability Margins and Disturbance Rejection Performance," presented at the American Helicopter Society 65th Annual Forum, Grapevine, TX, 2009.

<sup>16</sup>Mansur, M. H., Lusardi, J. A., Tischler, M. B., and Berger, T., "Achieving the Best Compromise between Stability Margins and Disturbance Rejection Performance," presented at the American Helicopter Society 65th Annual Forum, Grapevine, TX, 2009.

<sup>17</sup>Skogestad, S. and Postlethwaite, I., *Multivariable Feedback Control: Analysis and Design*, John Wiley and Sons, Ltd, 2005.

<sup>18</sup>Åström, K. J. and Murray, R. M., *Feedback Systems: An Introduction for Scientists and Engineers*, Princeton University Press, 2008.

<sup>19</sup>Hayes, P. M., Grill, I., and Horn, J., "Gust Rejection Using Active Trailing Edge Flaps," presented at the American Helicopter Society 68th Annual Forum, Fort Worth, Texas, 2012.